Supplementary Materials: Influence of MoS_2 on Activity and Stability of Carbon Nitride in Photocatalytic Hydrogen Production

Ramesh P. Sivasankaran [1], Nils Rockstroh [1], Carsten R. Kreyenschulte [1], Stephan Bartling [1], Henrik Lund [1], Amitava Acharjya [2], Henrik Junge[1], Arne Thomas [2] and Angelika Brückner [1,*]

Table S1: Synthesis method, reaction conditions and H_2 production rates of selected MoS_2/C_3N_4 based photocatalysts.

No.	Catalyst	Synthesis method	Optimum amount of MoS_2/wt. %	Sacrificial agent	Light source	Incident light (nm)	Activity (μmol h^{-1} g^{-1})	Ref.
1	EB/MoS_x/g-C_3N_4	In-situ photodeposition	0.5	TEOA	400 W Hg	> 420	180	[1]
2	MoS_2/g-C_3N_4	In-situ photodeposition	2.89	TEOA	300 W Xe	> 400	252	[2]
3	Pt/MoS_2/g-C_3N_4	Sonochemical	0.5	Methanol	300 W Xe	> 400	231	[3]
4	MoS_2/mpg-C_3N_4	Impregnation & Sulfidation	0.2	Lactic acid	300 W Xe	420	1125	[4]
5	MoS_2/g-C_3N_4	Impregnation-sulfidation	0.5	Lactic acid	300 W Xe	> 420	1340	[5]
6	MoS_2/C_3N_4	Hydrothermal	4	TEOA	300 W Xe	> 420	90	[6]
7	Amorphous MoS_x/g-C_3N_4	Adsorption-in situ transformation	3	Lactic acid	3 W LED	420	273.1	[7]
8	1T MoS_2/g-C_3N_4	Solvothermal	0.2	Lactic acid	300 W Xe	-	949	[8]
9	1T MoS_2/ O-g-C_3N_4	Solvothermal	0.2	TEOA	300 W Xe	> 400	1842	[9]
10	MoS_2/py-C_3N_4	Hydrothermal	3	TEOA	300 W Xe	> 420	500	[10]
11	g-C_3N_4/Ag/MoS_2	Hydrothermal	-	TEOA	300 W Xe	> 420	104	[11]
12	Pt/MoS_2/C_3N_4	In-situ photodeposition		Lactic acid	300 W Xe	-	2342	This work
13	Pt/MoS_2/C_3N_4	In-situ photodeposition		Lactic acid	300 W Xe	> 420	232.6	This work

Table S2. Elemental composition of as-synthesized and used catalysts derived from CHNS and ICP-OES.

Sample	C (wt.%)	N (wt.%)	Mo^{ICP} (wt.%)	S^{ICP} (wt.%)	Pt^{ICP} (wt.%)
2H MoS_2 (HT)			61.55	36.82	-
1T MoS_2 (ST)			48.64	33.67	-
2H MoS_2 (TD)			48.44	38.55	-
C_3N_4	31.99	61.75	-	-	-
2H MS-CN (PD)	30.96	56.81	0.85	0.74	-
2H MS-CN (SC)	30.46	57.13	1.04	0.70	-
1T MS-CN (SC)	30.56	57.27	0.88	0.61	-
2H MS-CN (TD)	31.69	58.20	1.0	0.79	-
MS-CN theoretically	*38.36*	*59.64*	*1.20*	*0.80*	-
Pt/CN			-	-	2.70
Pt/2H MS-CN (PD)			0.62	0.63	2.68
Pt/2H MS-CN (SC)			0.86	0.51	2.70
Pt/1T MS-CN (SC)			0.61	0.54	2.72
Pt/2H MS-CN (TD)			0.67	0.67	2.70

Table S3. Surface elemental composition of as-synthesized and used catalysts derived from XPS.

Sample	C (at.%)	N (at.%)	O (at.%)	Mo (at.%)	S (at.%)	S:Mo Ratio	Pt (at.%)	Pt^0 (at.%)	Pt^{2+} (at.%)
C_3N_4	44.67	52.59	2.74	-	-		-		
2H MS-CN (PD)	47.80	49.47	2.41	0.11	0.20	1.82	-		
2H MS-CN (TD)	41.42	55.34	2.65	0.15	0.46	3.07	-		
MS-CN theoretically[a]	*42.64*	*56.86*	-	*0.167*	*0.334*	*2*	-		
Pt/CN	46.05	48.93	4.12	-	-	-	0.90	0.66	0.24
Pt/CN theoretically[a]	*42.80*	*57.06*	-	-	-	-	*0.14*		
Pt/2H MS-CN (PD)	45.21	49.03	4.43	0.09	0.47	5.22	0.77	0.69	0.08
Pt/2H MS-CN (TD)	47.43	45.75	4.59	0.12	0.75	6.25	1.38	1.16	0.22

[a] calculated under the assumption that the elemental composition at the surface is the same as in the bulk.

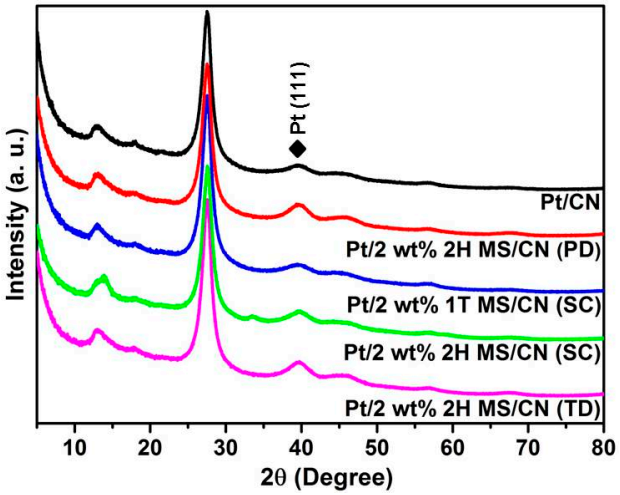

Figure S1. XRD powder patterns of Pt/CN and Pt/MS-CN composite catalysts removed from the reactor after 6 h irradiation under UV-vis light in the presence of lactic acid.

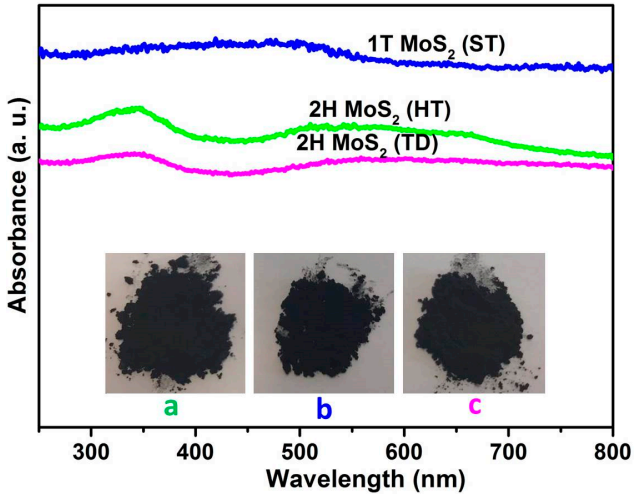

Figure S2. DRS UV-vis spectra of 2H MoS_2 (HT), 1T MoS_2 (ST) and 2H MoS_2 (TD). Photos: (a) 2H MoS_2 (HT), (b) 1T MoS_2 (ST) and (c) 2H MoS_2 (TD).

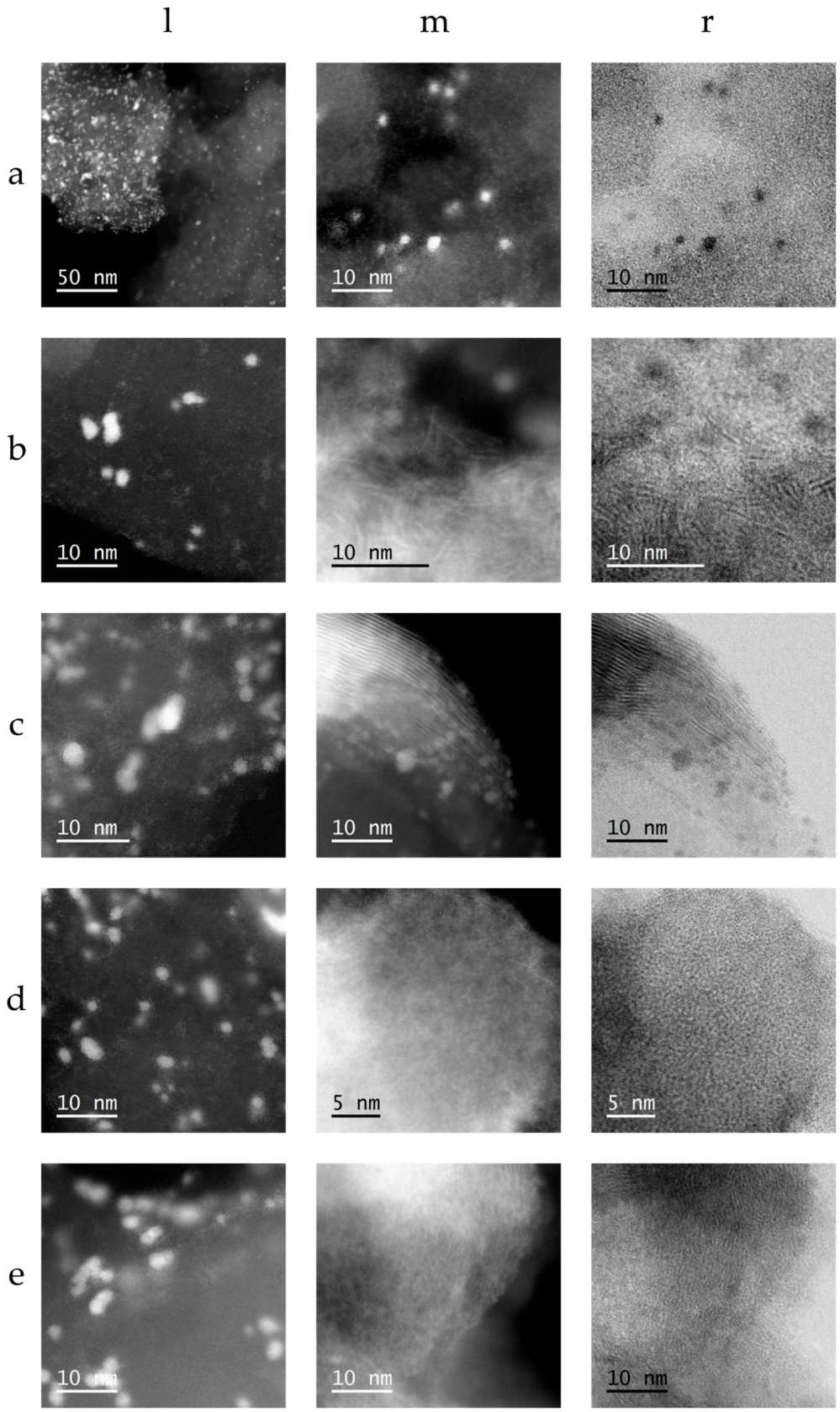

Figure S3. STEM high angle annular dark field (HAADF) micrographs of CN phase decorated with Pt (column l), high resolution HAADF (column m) and bright field (BF) micrographs (column r) of MoS_2 phase (when present) in catalysts exposed to UV-vis irradiation for 6 h in the presence of lactic acid; (line a) Pt/CN, (b) Pt/2H MS-CN (PD), (c) Pt/2H MS-CN (SC), (d) Pt/1T MS-CN (SC), (e) Pt/2H MS-CN (TD).

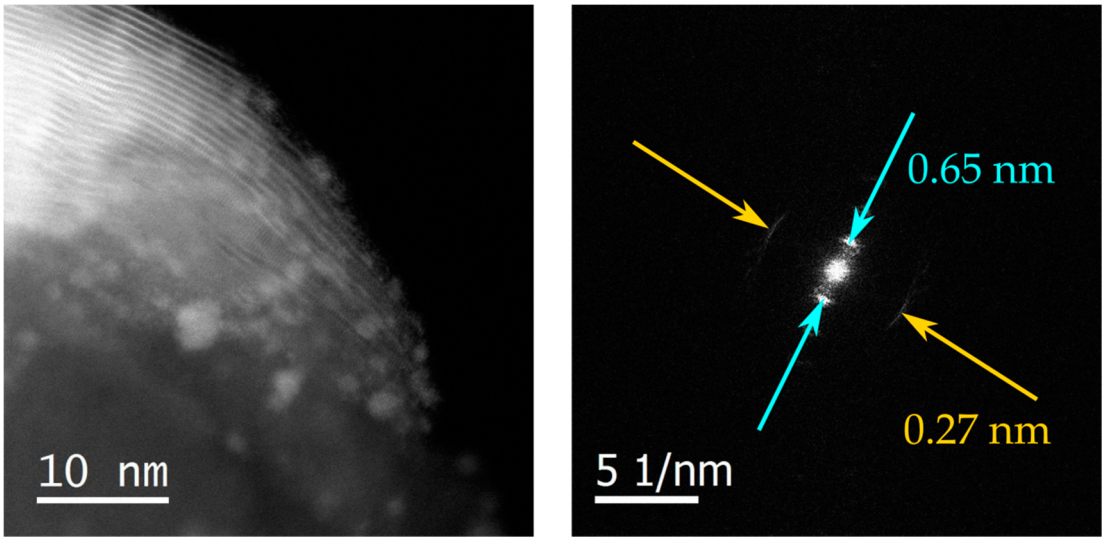

Figure S4. High resolution STEM-HAADF image with corresponding FFT of Pt/2H MS-CN (SC).

In Figure S4, the high resolution STEM-HAADF image of Pt/2H MS-CN (SC) illustrates that 2H MoS_2 has a typical layered structure. Analysis of the Fast Fourier Transformation (FFT) of that image revealed an interlayer spacing of 0.27 and 0.65 nm, which corresponds to the (100) and (002) planes of hexagonal 2H MoS_2 (ICDD: 01-075-1539) which also confirms the existence of 2H MoS_2 species in the composite catalysts.

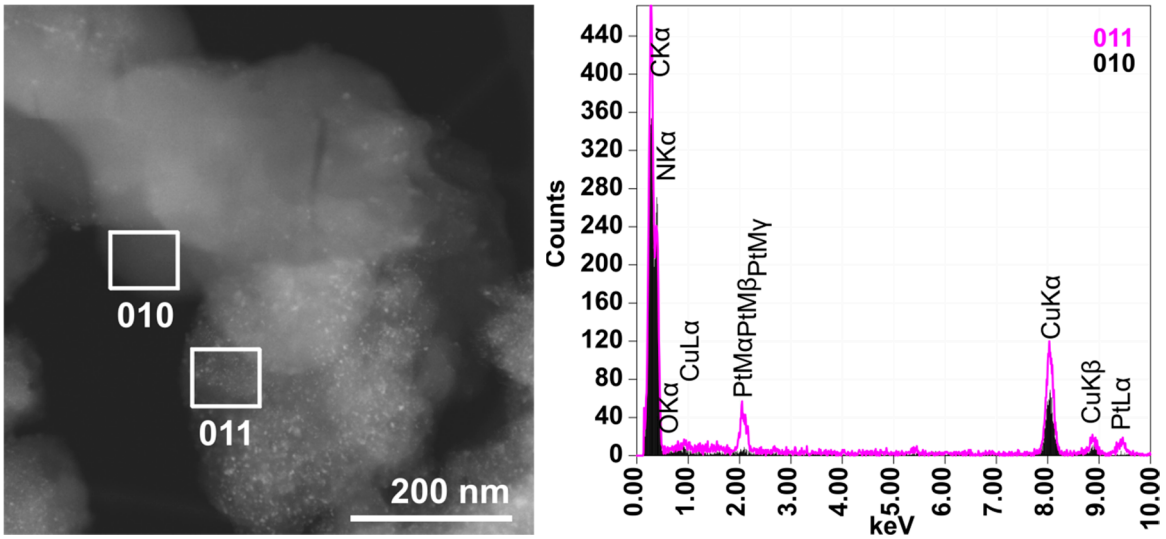

Figure S5. STEM-HAADF micrographs with corresponding EDX spectra of Pt/CN.

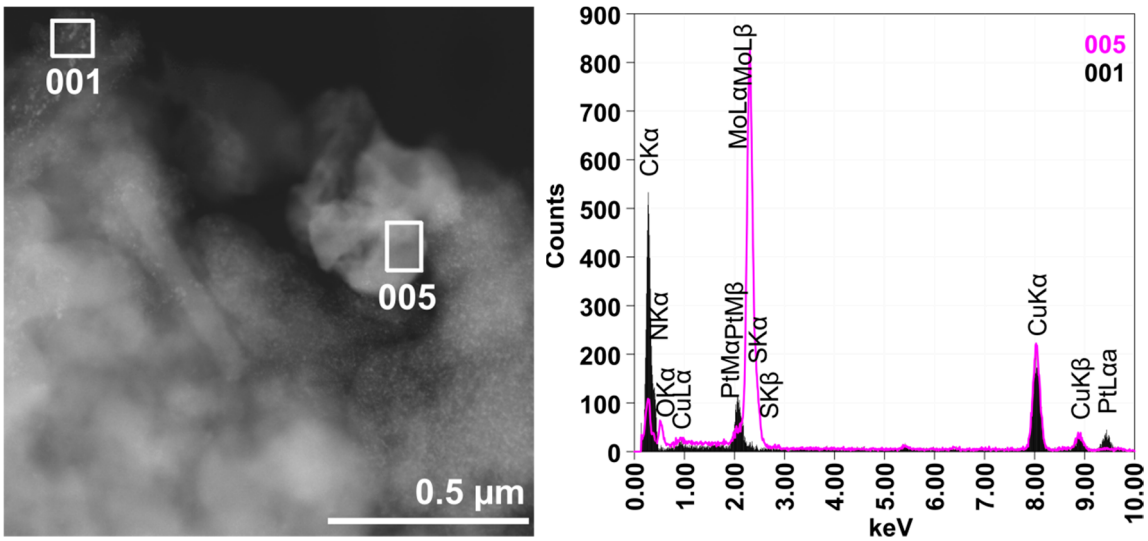

Figure S6. STEM-HAADF micrographs with corresponding EDX spectra of Pt/2H MS-CN (PD).

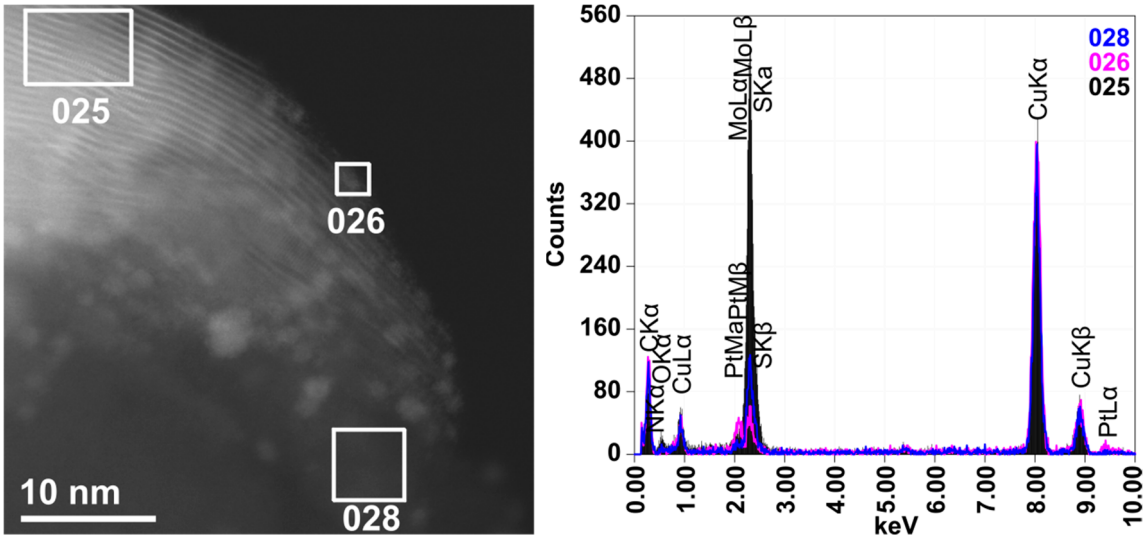

Figure S7. STEM-HAADF micrographs with corresponding EDX spectra of Pt/2H MS-CN (SC).

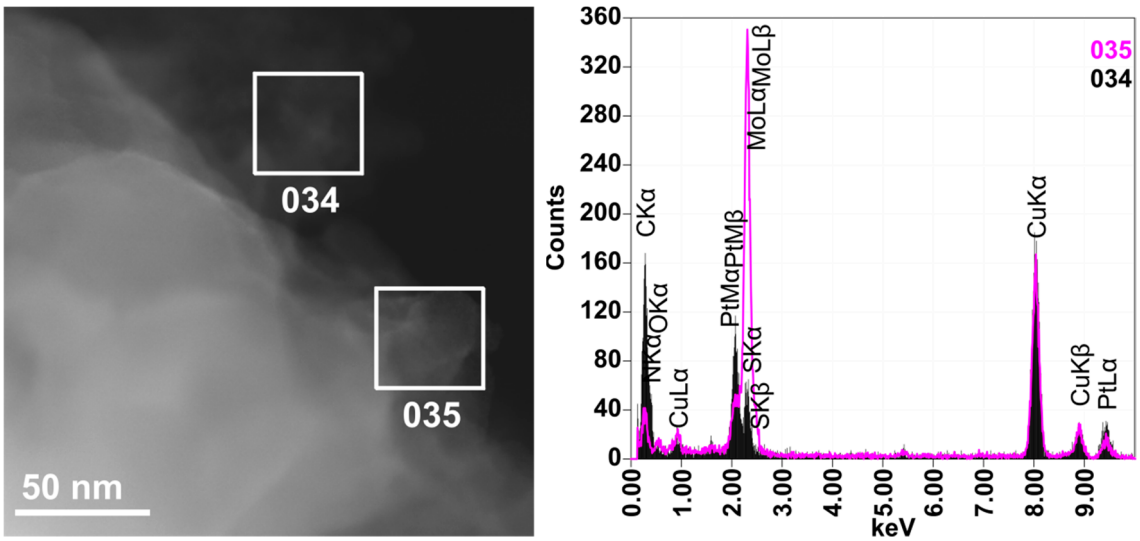

Figure S8. STEM-HAADF micrographs with corresponding EDX spectra of Pt/1T MS-CN (SC).

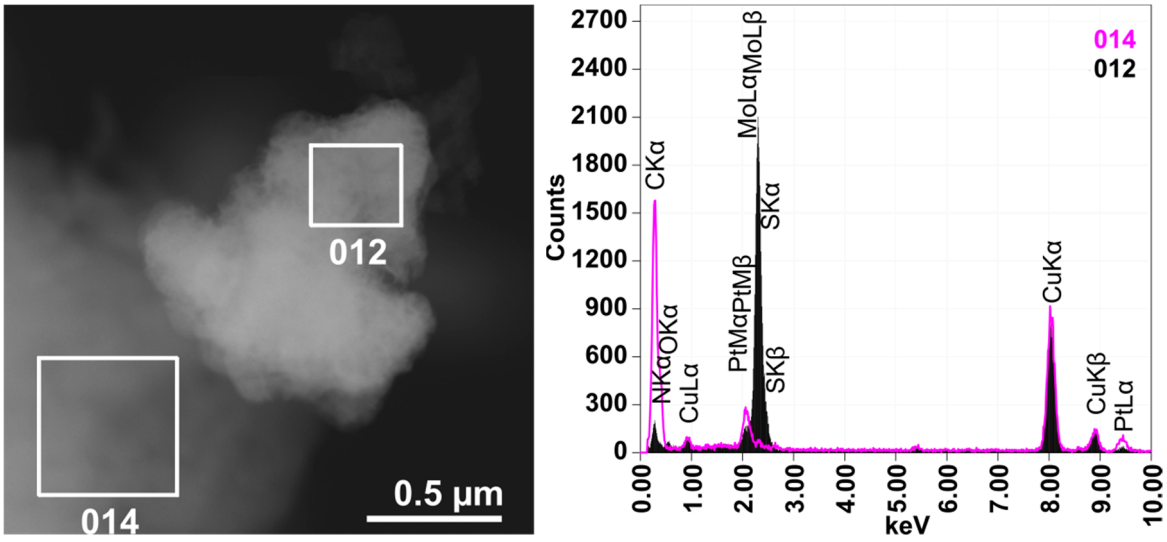

Figure S9. STEM-HAADF micrographs with corresponding EDX spectra of Pt/2H MS-CN (TD).

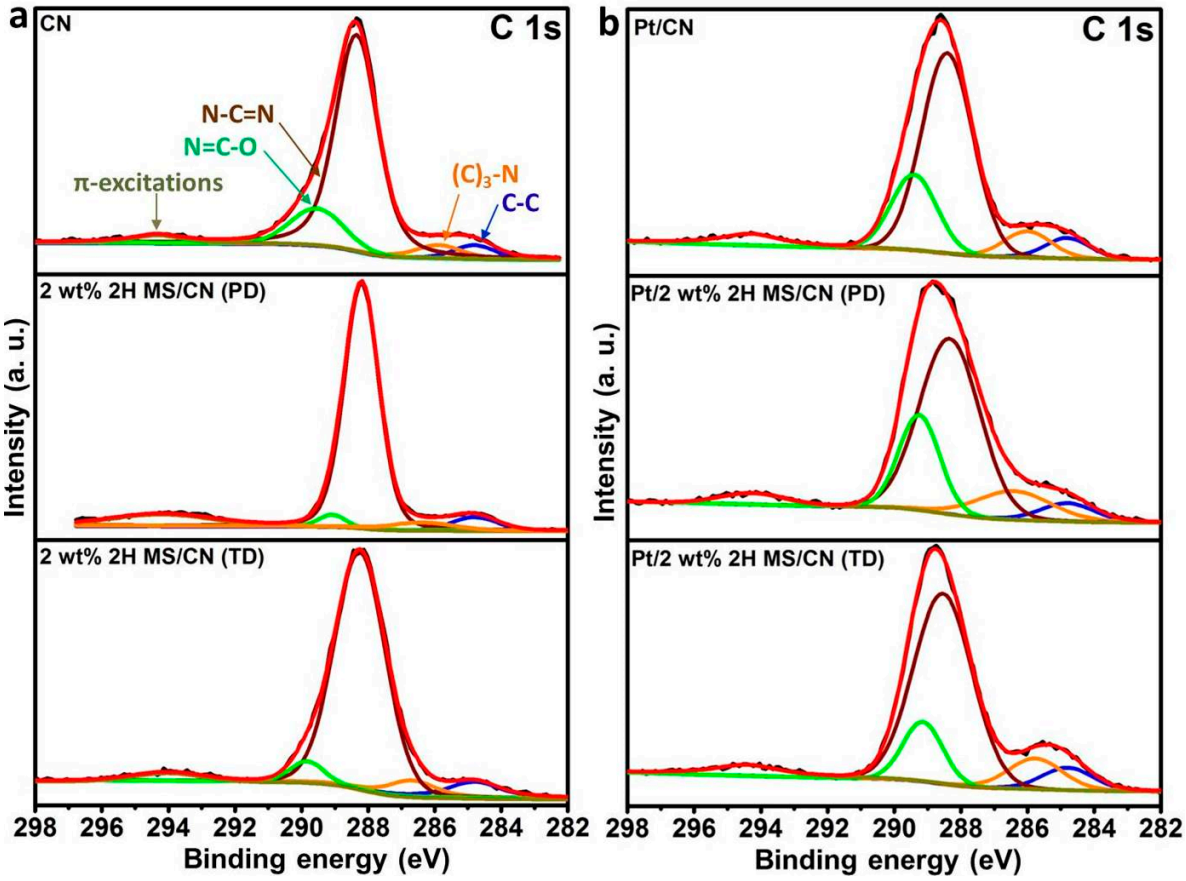

Figure S10. XP spectra of C 1s: (a) Fresh catalysts; (b) Recovered catalysts after 6h reaction.

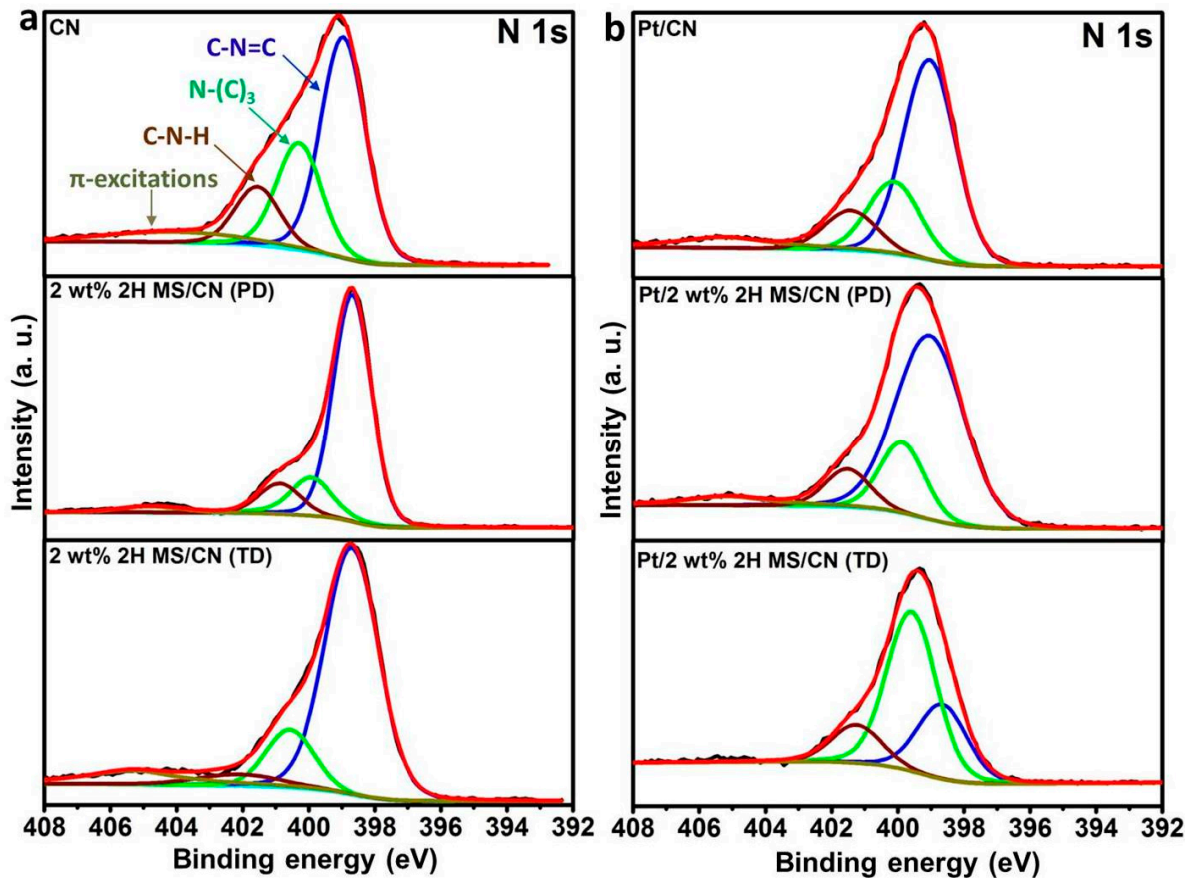

Figure S11. XP spectra of N 1s: (a) Fresh catalysts; (b) Recovered catalysts after 6h reaction.

The elemental C 1s spectrum of pure CN (Figure S10a, top) can be deconvoluted into four different peaks with binding energies centered at 289.5, 288.3, 285.9 and 284.8 eV. The peak located at 289.5 eV can be attributed to (N=C-O) groups, while the peak centered at 288.3 eV is associated with the sp^2-bonded carbon in an N-containing aromatic structure (N-C=N) which is the major carbon environment in the CN matrix. The peak at 285.9 eV is ascribed to carbon attached with tertiary nitrogen ($(C)_3$-N) and the peak at 284.8 eV corresponds to adventitious carbon species (C-C) (Figure S10a) [12]. The respective elemental N 1s spectrum of pure CN (Figure S11a, top) could be deconvoluted into three different peaks at binding energies of 401.5, 400.3 and 398.9 eV which can be assigned to the terminal amino groups (C-N-H), tertiary nitrogen groups ($N-(C)_3$) and sp^2-hybridized nitrogen involved in triazine rings (C-N=C), respectively [13]. Moreover, there is a weak peak present at 404.35 eV that is attributed to charging effects in CN (Figure S11a) [14,15].

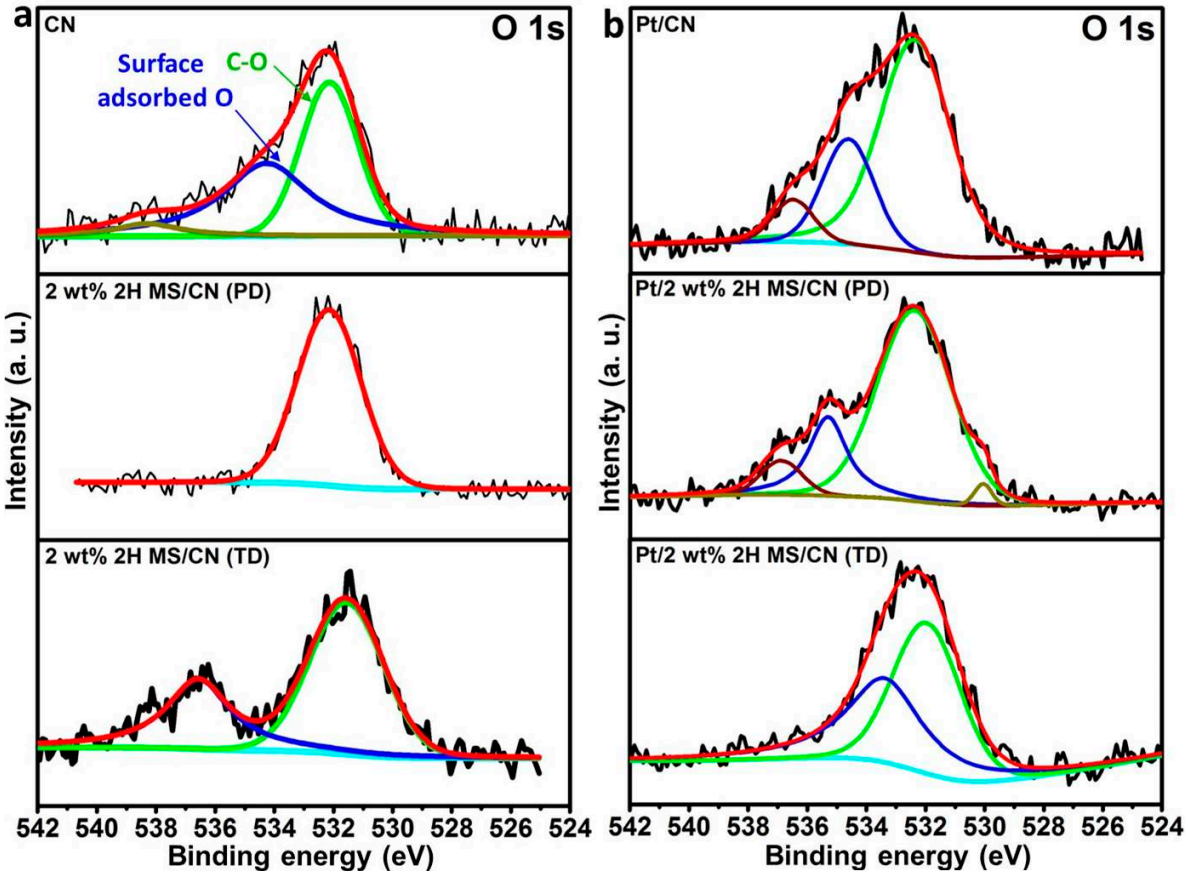

Figure S12. XP spectra of O 1s: (a) Fresh catalysts; (b) Recovered catalysts after 6h reaction.

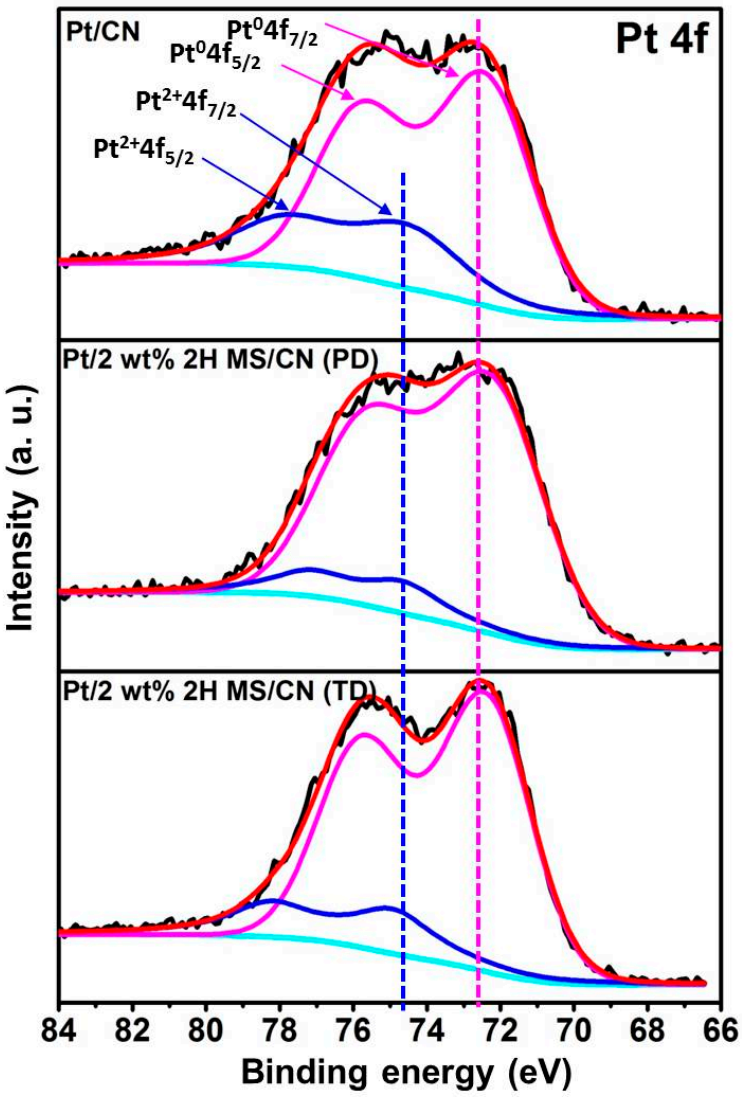

Figure S13. XP spectra of Pt 4f: Pt/CN, Pt/2H MS-CN (PD) and Pt/2H MS-CN (TD).

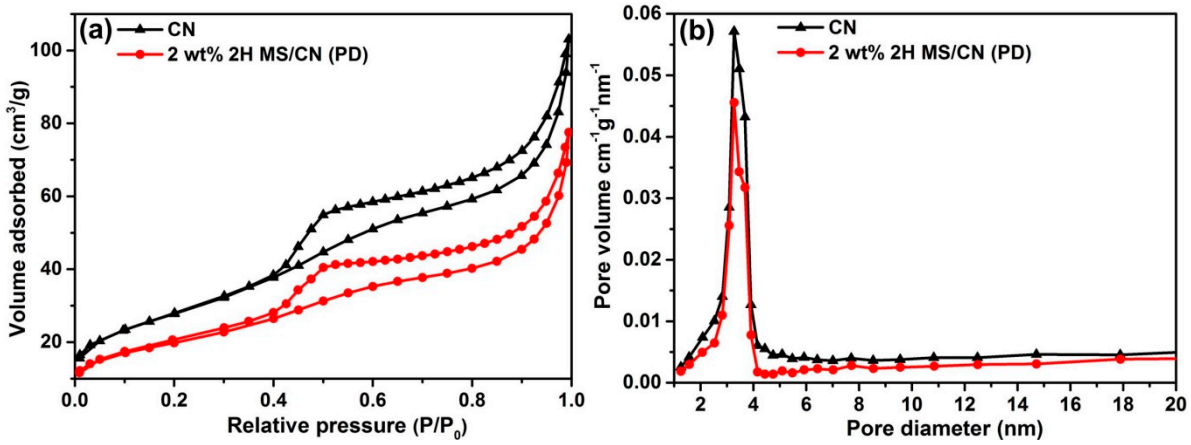

Figure S14. (a) N_2 adsorption-desorption isotherms of CN and 2H MS-CN (PD); (b) Barrett-Joyner-Halenda pore size distribution plot.

Table S4. Structural properties of as-prepared catalysts.

Sample	S_{BET} (m^2/g)	Pore volume (cm^3/g)	Mean pore size (nm)
C_3N_4	98.5	0.152	4.7
2H MS-CN (PD)	70.6	0.111	4.8
2H MS-CN (SC)	92.9	0.151	4.9
1T MS-CN (SC)	68.8	0.132	4.9
2H MS-CN (TD)	86.4	0.133	4.6

As shown in Fig. S14a, the pure CN and 2H MS-CN (PD) exhibited type IV isotherms with a H4 hysteresis loop, according to the IUPAC classification, indicating the existence of mesopores (2-50 nm). These H4 hysteresis loops indicate the formation of narrow slit-shaped pores. The specific surface area, pore volume and average pore size of the samples are summarized in Table S4. The pore size distribution of the samples were estimated by using the Barrett-Joyner-Halenda (BJH) method from the desorption branches, as shown in Fig. S14b.

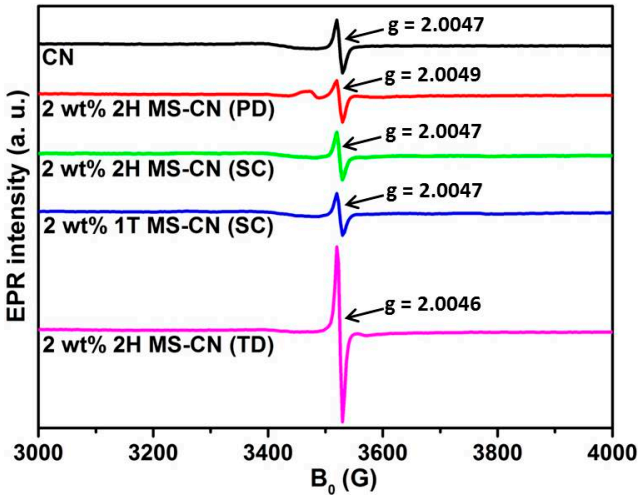

Figure S15. EPR signal of as synthesized catalysts at 300 K (without light irradiation).

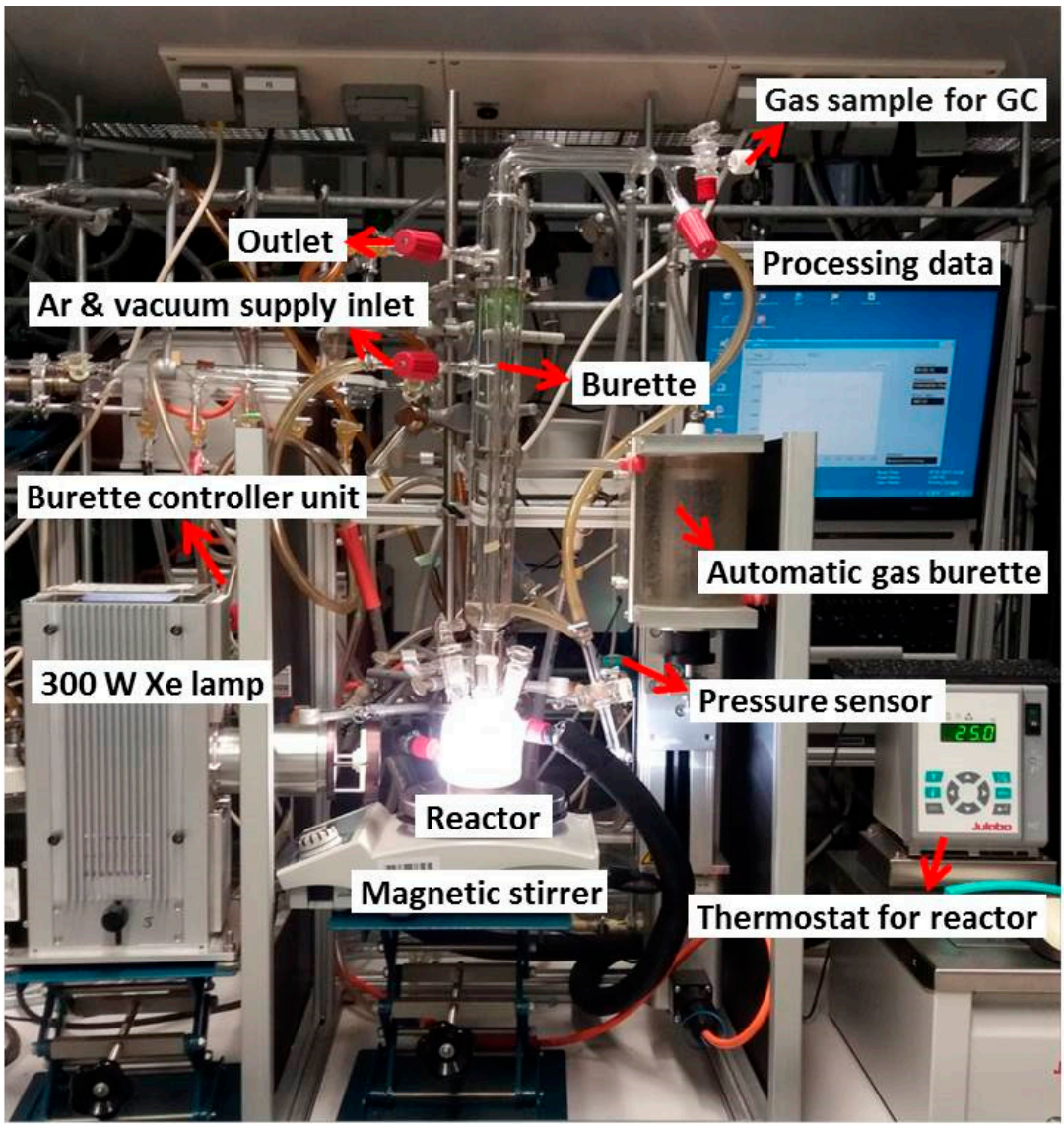

Figure S16. Experimental setup for photocatalytic H_2 production.

Discussion on Quantum Yield determination

The determination of quantum efficiencies is still subject of intense debate. This paragraph aims at providing issues that have to be considered in our eyes.

In a comprehensive article by Maschmeyer and Che it is shown that several possibilities exist to obtain the quantum efficiencies [16]. The most elegant is to conduct chemical actinometer experiments, which have been done for comparable systems in the same setup [17,18]. Comparison of these values with those obtained from measurements of the light intensity proved that only about 60% of the light irradiation entered the used reactor at selected wavelengths of 415 and 440 nm. Using this approach with 2H MS-CN and an irradiation wavelength of 415 nm gave quantum efficiencies of 1.43% (using a lamp output power of 1.5W) or 1.49% (using a lamp output power of 0.75W), respectively. These are lower compared with literature systems [19,20].

A more technical way to determine the quantum efficiency is comprised by the quotient of the enthalpy of combustion and the energy input. In the case of 2H MS-CN (PD) 1405.2 μmol of H_2 give an energy of about 402 J (based on upper heating value). The power of the irradiated light was 1.6 W giving an energy of 38.4 Wh or 138240 J in the period of 24 hours yielding a light-to-hydrogen efficiency of 0.29%. Considering that only 60% of the emitted light from the lamp entered the reactor, this value will be 0.48%.

The more proper way of calculation of QY would be the division of generated H atoms by incident photons. However, as there is no integration of the photon output spectrum of the Xenon lamp available, we can only take the number of photons, which are emitted by the sun in the range between 280 and 680 nm from literature [21], or the number of photons emitted by a mercury lamp at a medium wavelength of 440 nm and an output power of 1.0 W, which we measured ourselves (1.1×10^{18} per s and cm^2; these photons enter the reactor). Both values result in quantum yields of 1.41% and 1.11%, respectively. Although those are only rough estimations, they are in the same order of magnitude as the calculation based on the energy contents and somewhat lower than those determined directly. Nevertheless, we see the measurement/ determination of quantum yields critical as there are many other factors which have to be considered to obtain a good comparison between the results with other groups. This is also nicely reported by H. Kisch [22]. One issue is the wavelength used for the determination of the quantum yield. A common approach is the determination of the quantum yield at a single wavelength which shows this yield at this certain wavelength, but does neither provide information about quantum yields at other wavelengths (because different wavelengths could also cause different processes in the reactor) nor does it provide information about the sunlight-to-hydrogen-efficiency, because it is not the efficiency over the whole absorption range of sunlight. This is also reflected by our results that show a higher quantum efficiency at 415 nm in comparison to the value obtained by using the quotient of the enthalpy of combustion and the energy input. Another aspect is comprised by the concentrations used. If this is not in the saturation range of light absorption, a higher concentration would mean a higher reaction rate. Also, the reactive surface, that absorbs light may differ rendering quantum yields barely comparable. As an example, a solid with an "active absorption area" of 400 m^2/g and a quantum yield of 20% would provide 80 m^2, while another solid with an "active absorption area" of 100 m^2/g and a quantum yield of 50% would provide only 50 m^2 of effective absorption area. We would therefore be careful in using this parameter. Moreover, we used 1.6 W of photon intensity meaning an oversaturated system with respect to photons thus lowering the quantum yield. Another aspect caused by the concentration of the solid catalyst is the presence of other processes such as photon scattering and reflection. Moreover, there are many different setups that render comparison of quantum yields almost impossible. Nevertheless, conducting different reactions in the same setup would render results from different groups comparable. We think that such a measure would be appealing, but is not realizable at the current stage without considerable effort.

References:

1. Xu, J.; Li, Y.; Peng, S. Photocatalytic hydrogen evolution over Erythrosin B-sensitized graphitic carbon nitride with in situ grown molybdenum sulfide cocatalyst. *Int. J. Hydrog. Energy.* **2015**, *40*, 353-362.
2. Zhao, H.; Dong, Y.; Jiang, P.; Miao, H.; Wang, G.; Zhang, J. In situ light-assisted preparation of MoS_2 on graphitic C_3N_4 nanosheets for enhanced photocatalytic H_2 production from water. *J. Mater. Chem. A.* **2015**, *3*, 7375-7381.
3. Ge, L.; Han, C.; Xiao, X.; Guo, L. Synthesis and characterization of composite visible light active photocatalysts MoS_2–g-C_3N_4 with enhanced hydrogen evolution activity. *Int. J. Hydrog. Energy*. **2013**, *38*, 6960-6969.
4. Hou, Y.; Laursen, A. B.; Zhang, J.; Zhang, G.; Zhu, Y.; Wang, X.; Dahl, S.; Chorkendorff, I. Layered nanojunctions for hydrogen-evolution catalysis. *Angew. Chem. Int. Ed.* **2013**, *52*, 3621-5.
5. Zheng, D.; Zhang, G.; Hou, Y.; Wang, X., Layering MoS_2 on soft hollow g-C_3N_4 nanostructures for photocatalytic hydrogen evolution. *Appl. Catal. A.* **2016**, *521*, 2-8.
6. Gu, Q.; Sun, H.; Xie, Z.; Gao, Z.; Xue, C. MoS_2-coated microspheres of self-sensitized carbon nitride for efficient photocatalytic hydrogen generation under visible light irradiation. *Appl. Surf. Sci.* **2017**, *396*, 1808-1815.
7. Yu, H.; Xiao, P.; Wang, P.; Yu, J. Amorphous molybdenum sulfide as highly efficient electron-cocatalyst for enhanced photocatalytic H_2 evolution. *Appl. Catal. B.* **2016**, *193*, 217-225.
8. Wu, C.; Fang, Q.; Liu, Q.; Liu, D.; Wang, C.; Xiang, T.; Khalil, A.; Chen, S.; Song, L. Engineering interfacial charge-transfer by phase transition realizing enhanced photocatalytic hydrogen evolution activity. *Inorg. Chem. Front.* **2017**, *4*, 663-667.
9. Xu, H.; Yi, J.; She, X.; Liu, Q.; Song, L.; Chen, S.; Yang, Y.; Song, Y.; Vajtai, R.; Lou, J.; Li, H.; Yuan, S.; Wu, J.; Ajayan, P. M. 2D heterostructure comprised of metallic 1T-MoS_2 /Monolayer O-g-C_3N_4 towards efficient photocatalytic hydrogen evolution. *Appl. Catal. B.* **2018**, *220*, 379-385.
10. Li, M.; Zhang, L.; Fan, X.; Wu, M.; Du, Y.; Wang, M.; Kong, Q.; Zhang, L.; Shi, J. Dual synergetic effects in MoS_2/pyridine-modified g-C_3N_4 composite for highly active and stable photocatalytic hydrogen evolution under visible light. *Appl. Catal. B.* **2016**, *190*, 36-43.
11. Lu, D.; Wang, H.; Zhao, X.; Kondamareddy, K. K.; Ding, J.; Li, C.; Fang, P. Highly Efficient Visible-Light-Induced Photoactivity of Z-Scheme g-C_3N_4/Ag/MoS_2 Ternary Photocatalysts for Organic Pollutant Degradation and Production of Hydrogen. *ACS Sustainable Chem. Eng.* **2017**, *5*, 1436-1445.
12. Ech-chamikh, E.; Essafti, A.; Ijdiyaou, Y.; Azizan, M. XPS study of amorphous carbon nitride (a-C:N) thin films deposited by reactive RF sputtering. *Sol. Energy Mater. Sol. Cells.* **2006**, *90*, 1420-1423.
13. Indra, A.; Acharjya, A.; Menezes, P. W.; Merschjann, C.; Hollmann, D.; Schwarze, M.; Aktas, M.; Friedrich, A.; Lochbrunner, S.; Thomas, A.; Driess, M. Boosting Visible-Light-Driven Photocatalytic Hydrogen Evolution with an Integrated Nickel Phosphide-Carbon Nitride System. *Angew.Chem.* **2017**, *129*, 1675-1679.
14. Thomas, A.; Fischer, A.; Goettmann, F.; Antonietti, M.; Müller, J.-O.; Schlögl, R.; Carlsson, J. M. Graphitic carbon nitride materials: variation of structure and morphology and their use as metal-free catalysts. *J. Mater. Chem.* **2008**, *18*, 4893-4908.
15. Long, B.; Lin, J.; Wang, X. Thermally-induced desulfurization and conversion of guanidine thiocyanate into graphitic carbon nitride catalysts for hydrogen photosynthesis. *J. Mater. Chem. A.* **2014**, *2*, 2942-2951.
16. Maschmeyer, T.; Che, M. Catalytic Aspects of Light-Induced Hydrogen Generation in Water with TiO_2 and Other Photocatalysts: A Simple and Practical Way Towards a Normalization? *Angew. Chem. Int. Ed.* **2010**, *49*, 1536-1539.
17. Rosas-Hernández, A.; Alsabeh, P. G.; Barsch, E.; Junge, H.; Ludwig, R.; Beller, M. Highly active and selective photochemical reduction of CO2 to CO using molecular-defined cyclopentadienone iron complexes. *Chem. Commun.* **2016**, *52*, 8393-8396.
18. Alsabeh, P. G.; Rosas-Hernández, A.; Barsch, E.; Junge, H.; Ludwig, R.; Beller, M. Iron-catalyzed photoreduction of carbon dioxide to synthesis gas. *Catal. Sci. Technol.* **2016**, *6*, 3623-3630.
19. Lin, L.; Ou, H.; Zhang, Y.; Wang, X. Tri-*s*-triazine-Based Crystalline Graphitic Carbon Nitride for Highly Efficient Hydrogen Evolution Photocatalysis. *ACS Catal.* **2016**, *6*, 3921-3931.
20. Zhang, G.; Lin, L.; Li, G.; Zhang, Y.; Savateev, A.; Zafeiratos, S.; Wang, X.; Antonietti, M. Ionothermal Synthesis of Triazine–Heptazine-Based Copolymers with Apparent Quantum Yields of 60% at 420 nm for Solar Hydrogen Production from "Sea Water". *Angew. Chem. Int. Ed.* **2018**, *57*, 9372-9376.

21. Hambourger, M; Moore, G. F.; Kramer, D. M.; Gust, D.; Moore, A. L.; Moore, T. A. Biology and technology for photochemical fuel production. *Chem. Soc. Rev.* **2009**, *38*, 25-35.
22. Kisch, H. On the Problem of Comparing Rates or Apparent Quantum Yields in Heterogeneous Photocatalysis. *Angew. Chem. Int. Ed.* **2010**, *49*, 9588-9589.